Canadian Journal of Earth Sciences

OPEN ACCESS | Research Article

# Crustal stress near the Yakutat microplate collision from probabilistic earthquake focal mechanisms

**Jeremy M. Gosselin**[a], **Katherine M. Biegel**[b], **Jan Dettmer**[b], **Hersh Gilbert**[b], **Maurice Colpron**[c], **and Eva Enkelmann**[b]

[a]Natural Resources Canada, Geological Survey of Canada - Pacific, Sidney, BC, Canada; [b]Department of Earth, Energy, and Environment, University of Calgary, Calgary, AB, Canada; [c]Yukon Geological Survey, Whitehorse, YK, Canada

Corresponding author: **Jan Dettmer** (email: jan.dettmer@ucalgary.ca)



## Abstract

Earthquake source characteristics provide a valuable constraint on crustal stress and regional plate tectonics. Earthquake source studies in Yukon and northern British Columbia have been limited by sparse seismic network coverage. In this work, we leverage recent seismic network improvements to estimate focal mechanisms for small- and moderate-magnitude ($M >$ 2.0) earthquakes from P-wave first-motion polarity data. We invert these data within a probabilistic framework to rigorously quantify mechanism uncertainties. Subsequently, probabilistic earthquake focal mechanisms are used as input for inversions for the orientation of principal stress axes, and stress shape ratio, for spatial windows throughout the region. We implement a novel, data-driven approach to propagate focal mechanism uncertainty in stress inversion. Our results improve the spatial coverage of existing earthquake focal mechanisms and enable an orogenic-scale study of crustal stress near the Yakutat–North America collision. Overall, the region is characterized by a transpressive stress regime. Maximum horizontal compressive stress orientations exhibit a pattern orthogonal to the Yakutat collision syntaxis. Stress inversion results also reveal an abrupt change in orientation east-to-west, which we interpret as a change in stress regime across the Fairweather–Connector–Totschunda fault system that is likely related to coupling between the subducting Yakutat slab and North America. This work improves our understanding of potential earthquake hazards in southwestern Yukon and the surrounding region.

**Key words:** tectonics, earthquake focal mechanisms, crustal stress, Yukon, Alaska

## 1. Introduction

Southwest Yukon and southeast Alaska are characterized by the ongoing oblique collision of the Yakutat microplate with North America (Fig. 1). Here, the active plate boundary changes from the Fairweather transform to the Chugach–St. Elias thrust fault, creating a complex pattern of deformation and uplift that resulted in the highest coastal mountain range on Earth with >5000 m high peaks surrounded by fast-moving glaciers. This natural laboratory attracted much research in the interplay between tectonics and surface processes. Particular focus has been on the Alaska side of the St. Elias Mountains where the incoming Yakutat microplate and its sedimentary cover deforms onshore and offshore as material is carried into and through the plate corner (e.g., Bruhn et al. 2012; Enkelmann et al. 2015; Worthington et al. 2018). What is much less known, is how stress is transported inboard of the plate boundary—in southwest Yukon and northwest British Columbia.

Earthquake source characteristics can help constrain current crustal stress. Yet, most studies on earthquake source characteristics in southwestern Yukon predate significant seismic network improvements, and so generally only consider few of the largest events (e.g., Ristau et al. 2007; Ruppert 2008; Ekström et al. 2012; Kao et al. 2012; Doser 2014). In the last decade, seismic network improvements reduced the magnitude of completeness of the earthquake catalog in southwestern Yukon from ~3.0 to approximately ~1.0, and reduced systematic earthquake location (horizontal) errors by up to tens of kilometres (Meighan et al. 2013). The temporary Earthscope Transportable Array (Busby and Aderhold 2020) and Mackenzie Mountain (Baker et al. 2020) projects further reduced earthquake detection thresholds and location errors (Ruppert and West 2020). Previous studies of crustal stress based on earthquake source properties in this region (Ruppert 2008) predate seismic network improvements, which are summarized in Fig. S1.

In this work, we present probabilistic focal mechanism estimates for several hundred small-magnitude ($M >$ 2.0) earthquakes in southeast Alaska, southwest Yukon, and northwest British Columbia. Focal mechanisms were estimated from P-wave first-motion polarity measurements, which leverage recent seismic network improvements. Focal mechanisms were subsequently used as input for inversions of crustal stress orientations and shape ratios. We implement a novel, data-driven approach to propagate focal mechanism uncertainty in stress inversion. Our results significantly improve upon the spatial resolution of available seismological estimates of crustal stress, and resolve spatial variations in stress

**Fig. 1.** Tectonic setting of the Yakutat microplate collision near southwestern Yukon. Major faults are shown as blue lines. Faults discussed in the text are labelled: Denali fault (DF); Totschunda fault (TF); Border Ranges fault (BRF); Duke River fault (DRF). The inferred Connector fault (CF) is shown as a dashed blue line. The surface extent of the Yakutat microplate (Yak) and the active plate boundaries of the Fairweather fault (FF) and Chugach–St. Elias fault (CSEF) are delineated by red lines. The transparent red polygon, and dashed red line, approximately delineates the subsurface extent of the subducting Yakutat slab based on seismic tomography (Eberhart-Phillips et al. 2006) and plate kinematics (Pavlis et al. 2019), respectively. The black dotted lines represent the depth to the top of the subducting slab (labels in km; Hayes et al. 2018). The red dashed box defines the study area shown in subsequent figures. Locations of Holocene and Pleistocene volcanoes are shown as red triangles (Global Volcanism Program 2024). The inset map provides large-scale tectonic context of the interaction between the Pacific plate (PA), North American plate (NA), and Yakutat microplate (Yak). The region is characterized by a transition from the transform FF and Queen Charlotte fault (QCF) to the Aleutian subduction zone (ASZ). The black box in the inset map shows the approximate extent of the main map. Plate boundaries in the inset map are shown in blue. The black arrows in both maps illustrate the plate motion vectors relative to NA (Kreemer et al. 2014). Political boundaries in both maps are shown in black. Figure basemap obtained from ArcGIS mapserver (Esri 2024). Map shown in Albers projection, WGS84 datum, and latitude–longitude coordinates.

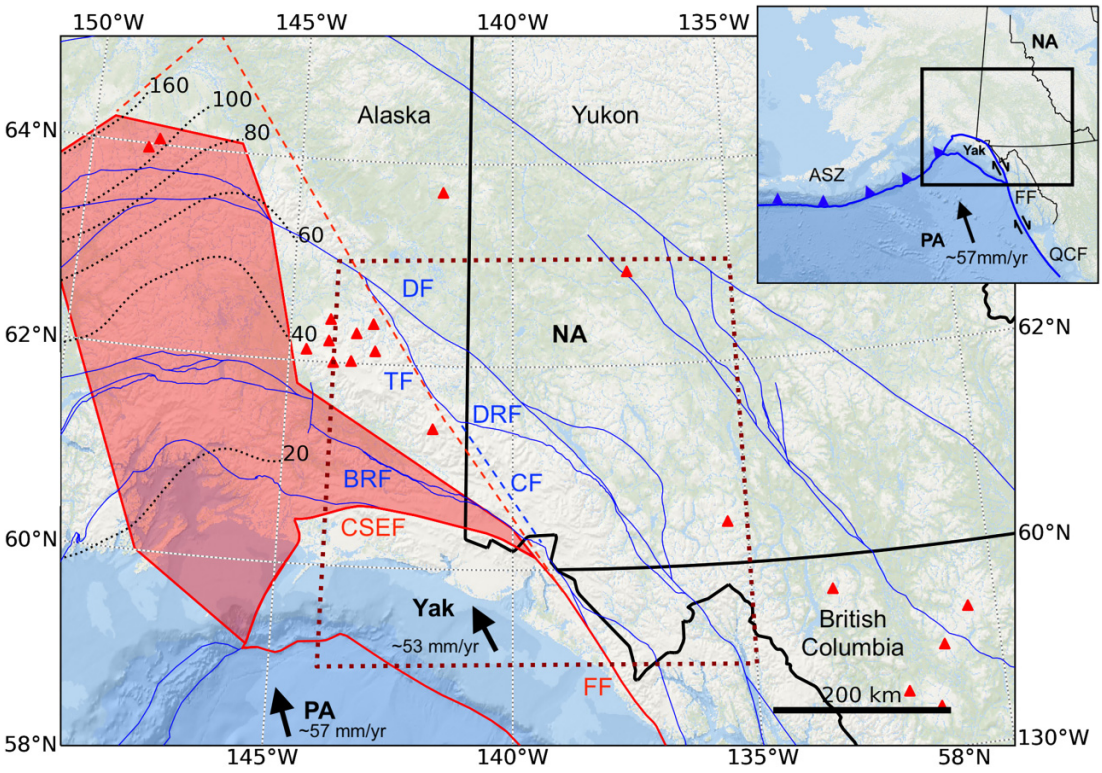


orientations at an orogenic scale. We show how crustal stresses change from reverse to strike–slip-dominated deformation in the inboard region between the Fairweather–Connector–Totschunda fault and the eastern Denali fault.

## 1.1. Tectonic setting

The Yakutat microplate is a thick, buoyant oceanic plateau (Fig. 1; Christeson et al. 2010) that causes flat-slab subduction (Eberhart-Phillips et al. 2006) and surface uplift in southern Alaska since ~36 Ma (Finzel et al. 2011). The ongoing oblique collision of the Yakutat plate corner in southeast Alaska resulted in rapid uplift and exhumation of the St. Elias Mountains (Enkelmann et al. 2008, 2009; Koons et al. 2022). The Yakutat microplate is connected with the Pacific plate that is moving northward along the Queen Charlotte–Fairweather transform fault system at the western margin of North America (Fig. 1 inset). In the north, subduction of the Pacific plate forms the Alaska–Aleutian Subduction zone. The tectonic regime of southwestern Yukon and southeastern Alaska is characterized by the transition between these boundary styles and the buoyant Yakutat crust (Plafker 1987; Leonard et al. 2007). In addition to significant coastal uplift, regional plate motion is partitioned between convergence as well as a series of right-lateral strike–slip fault systems (Bruhn et al. 2012).

The geology of southeast Alaska and southwest Yukon comprises the amalgamation of far-travelled terranes, which, collectively, form the northern North American Cordillera (Nelson et al. 2013). This includes, from northeast to southwest in the study area, the Yukon–Tanana terrane, the Insular Superterrane, the Chugach accretionary complex, and the actively colliding Yakutat terrane (Plafker 1987; Nelson et al. 2013). The Denali and Border Ranges faults represent sutures bounding the Insular Superterrane to the northeast

and southwest, respectively. Within the Insular Superterrane, the Duke River fault separates rocks of the Wrangellia and Alexander terranes (Fig. 1). Active deformation in southwest Yukon is characterized by a network of interacting crustal faults located southwest of the Denali fault (Fig. 1; Biegel et al. 2024). The Denali fault spans >2000 km from northwest British Columbia through southwest Yukon and the entirety of central Alaska. It has experienced 400-480 km of displacement since ~57 Ma (Eisbacher 1976; Lowey 1998). Quaternary fault mapping, geomorphology, and geodetic constraints suggest that the Denali fault is more active in central Alaska than Yukon; with slip rates ranging from >5 mm/year (central Alaska) to <1 mm/year (Yukon) (Bemis et al. 2015; Marechal et al. 2015, 2018). This is further supported by estimates of tectonic deformation rates derived from GPS data (e.g., Leonard et al. 2007, 2008).

Much of the Denali fault through southwestern Yukon is currently seismically quiescent (Fig. S2), and the majority of recorded seismicity occurs in the ~100 km wide corridor between the active Fairweather transform and the eastern Denali fault (Biegel et al. 2024; Han et al. 2024). The M7.9 Denali earthquake in 2002 ruptured the central Denali fault in central Alaska, then propagated southeastward along the Totschunda fault (Fig. 1) instead of continuing along the Denali fault through southwestern Yukon (Eberhart-Phillips et al. 2003). These observations contribute to recent studies that propose the Denali fault system serves as a regional stress boundary (Choi et al. 2021). This is supported by thermochronology studies that suggest much more recent exhumation southwest of the eastern Denali fault than north of it (Enkelmann et al. 2017; McDermott et al. 2019; Enkelmann and Falkowski 2021). Furthermore, it is suggested that the inferred Connector fault (Fig. 1) provides a structural link that accommodates and transfers strain between the Fairweather and Totschunda faults (Richter and Matson Jr. 1971; Lahr and Plafker 1980; Doser 2014). Spatial variations in deformation rates inferred from GPS measurements require motion along the Connector fault (Elliott and Freymueller 2020). Despite direct field observation/mapping being unavailable due to glaciation and inaccessibility, recent relocation of regional seismicity delineates the Connector fault (Fig. S1) and provides strong evidence in support of its active role in explaining regional deformation (Biegel et al. 2024). The Fairweather–Connector–Totschunda fault system enables strain transfer that likely bypasses the Denali fault in southwest Yukon. Yet, geological and geomorphological evidence suggests the Denali fault is active in this region (e.g., Blais-Stevens et al. 2020; Finley et al. 2021), with the potential for large earthquakes.

## 2. Data and methods

### 2.1. Earthquake focal mechanisms

Seismic station network coverage throughout southeastern Alaska and southwestern Yukon has improved significantly in recent years. Our work uses all available data from permanent and temporary regional networks to estimate detailed seismological constraints on the crustal stress field throughout the region. We consider earthquakes from the United States Geological Survey catalog as it is continuous over our study region, which extends through southeastern Alaska. The majority of the events in this catalog are contributed by the Alaska Earthquake Centre (AEC, Alaska Earthquake Center 1987). Specifically, we attempt to estimate focal mechanisms for earthquakes in our study region between 2010 and 2022, with magnitudes above 2. Since the purpose of this study is to constrain crustal stress in the North American plate, we consider only events shallower than 30 km throughout our study region. Furthermore, we do not consider offshore events or events near the coast (with latitude <60.5° and longitude <−139.0°) with depths exceeding 12 km, which are likely within the downgoing Yakutat slab (Hayes et al. 2018). However, it is possible that some of the events considered in our work occurred within the downgoing plate, but are retained due to large depth errors or analyst–fixed depths within the catalog.

For each selected event, we downloaded available vertical-channel waveform data for stations within 450 km epicentral distance. After applying a 1 Hz high-pass filter, we manually selected first-motion polarities for stations with clear P-wave arrival onsets. For most events, clear P-wave arrivals are only reliably determined for stations within 200 km distance. Azimuth and takeoff angles were calculated using ray propagation through the AEC velocity model for southeastern Alaska (Alaska Earthquake Center 1987; Fogleman et al. 1993). Finally, for events with greater than 10 measurements, polarities were inverted to estimate earthquake focal mechanisms within a probabilistic framework (Gosselin et al. 2022; Hamidbeygi 2022) using the Bayesian Earthquake Analysis Tool (BEAT; Vasyura-Bathke et al. 2020). The probabilistic approach to earthquake focal mechanism estimation allows for rigorous quantification of uncertainties, which enables more reliable interpretations of fault behaviour, crustal stress and, ultimately, regional tectonics.

Applications of Bayesian inversion in seismic source studies is established (see Vasyura-Bathke et al. 2020, and reference therein). Within this framework, model parameters and data are treated as random variables. Here, the model parameters are the strike, dip, and rake of the earthquake focal mechanism, and are constrained by data (P-wave polarities) as well as prior information. For some problems, prior information can be informative (providing additional constraint) or uninformative (allowing the solution to be constrained by data information). Specifically, Bayesian inversion uses data to update the prior knowledge of the model parameters. This determines the posterior probability density (PPD) of the model parameters, which represents the solution to the inverse problem (Jaynes 2003). The prior and PPD are related through Bayes' theorem, which is given by

$$P(\mathbf{m}|\mathbf{d}) = \frac{P(\mathbf{m})\,P(\mathbf{d}|\mathbf{m})}{P(\mathbf{d})}, \quad (1)$$

where $\mathbf{d}$ and $\mathbf{m}$ are vectors of data and model parameters, respectively. $P(\mathbf{m}|\mathbf{d})$ is the conditional probability of the model parameters given the data, which is the PPD. $P(\mathbf{m})$ is the prior probability density of the model parameters, independent

of the data. In this study, priors are uniform distributions bounded by the physical limits of strike, dip, and rake. $P(\mathbf{d}|\mathbf{m})$ is the conditional probability of the data given the model parameters. In practice, the data are a fixed realization of a random variable once they are measured/observed. This conditional probability therefore represents the likelihood $L(\mathbf{m})$ that a set of model parameters can reproduce the observed data. Finally, $P(\mathbf{d})$ provides a normalization independent of the model parameters. This is not required to be known in order to implement the numerical approach used in this study (MacKay 2003).

The likelihood function quantifies the probability that a particular set of model parameters gave rise to the data. It can be formulated based on the assumed statistical distribution of data errors, which are represented by the data residuals (i.e., the differences between predicted and measured P-wave polarities). The implementation in BEAT uses a likelihood function that assigns higher probability to arrivals that have a greater theoretical amplitude, depending on their takeoff location on the focal sphere (Brillinger et al. 1980). In theory, polarity data with takeoff locations near focal mechanism planes are less reliable due to potential modelling errors in takeoff locations (i.e., due to inaccurate event hypocenters, velocity models, etc.). These measurements will also be based on manual first-motion polarity assignment of lower signal-to-noise ratio (SNR) waveforms, relative to measurements with takeoff locations further from the true mechanism planes. Assuming independent polarity measurements, the likelihood is given by

$$L(\mathbf{m}) = \prod_{i=1}^{N} \phi_i^{\frac{1+d_i}{2}} (1-\phi_i)^{\frac{1-d_i}{2}}, \tag{2}$$

where $d_i$ is the polarity datum measured at station $i$, and $\phi_i$ is given by

$$\phi_i = \gamma + (1-2\gamma)\,\Omega\left(\frac{A_i(\mathbf{m})}{\sigma}\right). \tag{3}$$

Here, $\Omega(\cdot)$ is the cumulative distribution function of the normal distribution, which provides an estimate of polarity probability given a theoretical amplitude $A_i(\mathbf{m})$ and modelling error standard deviation $\sigma$. $\gamma$ represents the probability of incorrect manual polarity assignment (i.e., $0 < \gamma < 0.5$) and can be considered small for high-quality (high SNR) waveforms. We assume a conservative probability of incorrect polarity assignment of $\gamma = 0.2$ that enables flexibility in the error model (see Hamidbeygi 2022, for details). Furthermore, we treat $\sigma$ as an unknown hyper-parameter that is estimated as part of the inversion. This provides additional flexibility in the representation of data errors, which is solved for as part of the inversion procedure. The prior probability of $\sigma$ is uniform and bounded between 0 and 0.2.

For many problems, it is challenging (and often impossible) to determine an analytical solution for the PPD (eq. 1). Instead, numerical methods are often used to draw samples from the PPD. The ensemble of samples can then be used to approximate the PPD to estimate its properties. The inversion method implemented in BEAT, and used in this study, estimates the PPD via a sequential Monte Carlo sampler (Del Moral et al. 2006). The samples are independent and based on a sequence of intermediate distributions (i.e., stages) that transition between the prior and posterior, controlled by a scaling parameter. Depending on the choice of prior, this implementation allows for wide (unrestricted) initial exploration of the parameter space, which then becomes more constrained by the data (via the likelihood function) as the inversion progresses towards the posterior. All inversions in this work are run with 2000 sampling chains with 300 steps each. The number of sequential stages is adapted according to the polarity dataset for each inversion (typically <5). See descriptions in Vasyura-Bathke et al. (2020) for details. BEAT is a highly flexible program that can consider many additional parameters, more complex source types, as well as other seismic and geodetic data types. For simplicity, this initial work considered only the three parameters required to define the earthquake focal mechanism. Future work will include more comprehensive use of BEAT capabilities for data from southwestern Yukon. See Hamidbeygi (2022) and Gosselin et al. (2022) for additional details on Bayesian focal mechanism inversion and data from southwestern Yukon.

We performed probabilistic focal mechanism inversions for 363 events in southwestern Yukon and the surrounding region (Fig. 2). Figure S3 shows an example of the results of Bayesian focal mechanism inversion for a single event. The uncertainty in focal mechanism solutions (described by the PPD) can be illustrated by the distribution of Kagan angles (Kagan 1991), which define the minimum angular separation between two focal mechanisms. In this case, Kagan angles are calculated relative to the maximum probability model (Fig. S4). Where available, earthquake hypocentre locations were updated using results from recent work that relocated regional seismicity (Biegel et al. 2024). This work demonstrated significant improvements in earthquake location constraints (particularly in depth). Figure S5 illustrates systematic improvements in Bayesian focal mechanism inversion results (specifically, reduced uncertainty) for events with updated hypocentre locations. Maximum probability focal mechanism solutions for all events considered in this study are illustrated in Fig. 2. These are categorized according to mechanism type as defined by Kaverina et al. (1996) and Álvarez-Gómez (2019). The figure shows the trends of the mechanism p-axes, which are generally consistent for proximal earthquakes. Also shown are available focal mechanisms for this region from the International Seismological Centre (ISC) catalog between 2000 and 2022 (Lentas et al. 2019). These are predominantly larger events that mostly predate major seismic network improvements. We use these additional events to augment our focal mechanism dataset for inferring regional tectonic stress. The region is characterized by mostly strike–slip and reverse faulting, consistent with observations from previous studies (e.g., Ristau et al. 2007; Ekström et al. 2012; Kao et al. 2012; Doser 2014). Our work improves the spatial density of focal mechanism estimates.

Many of the earthquakes considered in this work are small magnitude ($M < 2.5$) events with poorly constrained mechanisms (i.e., large focal mechanism uncertainties, see supple-

**Fig. 2.** Earthquake focal mechanisms in southwestern Yukon. Major faults are shown as blue lines. The inferred Connector fault is shown as a dashed blue line. (A) Earthquake focal mechanisms are classified according to Álvarez-Gómez (2019). Dark blue and yellow circles represent estimates from this study and the International Seismological Centre catalog (ISC; Lentas et al. 2019), respectively. (B) P-axis trends of reverse focal mechanisms from this study (black) and the ISC catalog (red). (C) and (D) show p-axis trends of normal and strike–slip mechanisms, respectively. Figure basemap obtained from ArcGIS mapserver (Esri 2024). Map projection, datum, and coordinates as in Fig. 1.

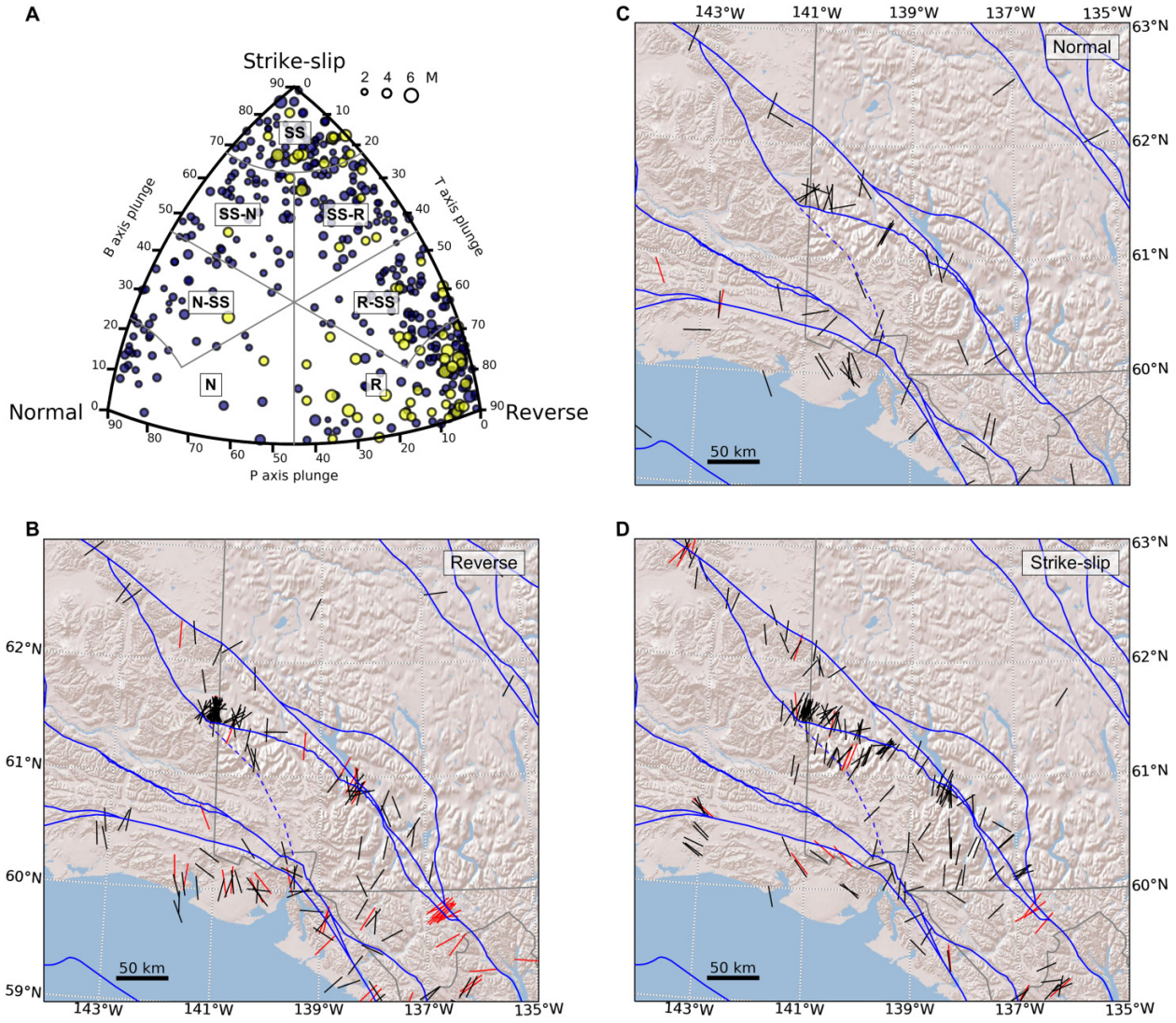


ment for details). However, these events still contribute valuable information for constraining crustal stress. In order to qualitatively assess the probabilistic focal mechanism inversion results, we first simulate the distribution of Kagan angles for various hypothetical focal mechanism uncertainty distributions (Fig. S6). Importantly, we simulate the distribution of Kagan angles expected for an unconstrained focal mechanism inversion where the PPD is equivalent to the prior uniform distribution (Fig. S6E). The posterior distributions of Kagan angles (relative to maximum probability models) for all events are shown in Fig. S7. The majority of events exhibit significantly improved constraint relative to the prior (i.e., narrower distributions of Kagan angles). This observation, as well as the spatial similarity in inferred p-axis trends (Fig. 2), provides confidence in these focal mechanism inversion results. We note that the estimated focal mechanism uncertainties exhibit some dependence on earthquake magnitude and spatial variability in station coverage (see supplement for details).

We augment our collection of focal mechanism estimates with the ISC catalog (Lentas et al. 2019). In order to assign conservative uncertainty estimates to these events (for use in subsequent stress inversions), we first established a relationship between focal mechanism uncertainty and earthquake magnitude using our probabilistic inversion results (Fig. S8). We then determined the width of a Gaussian distribution of rotations that reproduced this magnitude–uncertainty relation (Fig. S9). We expect that this relation may change according to study region and time (e.g., due to data quality, velocity model complexity, and seismic station distribution). Since all of the

events in the ISC catalog for this study region are greater than magnitude 3.0, the assigned focal mechanism uncertainties are small compared to our uncertainty estimates for smaller events. However, our assigned uncertainties for the event in the ISC catalog are likely overestimated, since many of these solutions are inferred from additional data and data types (e.g., waveforms).

## 2.2. Stress inversion

Earthquake focal mechanisms provide a valuable input for estimating tectonic stress. The P-axes of focal mechanisms are geometrical properties related to the individual earthquakes (Fig. 2), whereas the vector of principle crustal stress applies to a volume of rock and can activate faults with a variety of geometries (McKenzie 1969). Specifically, the principle stress vector lies within the pressure quadrant of an individual focal mechanism (McKenzie 1969). Methods for estimating tectonic stress generally assume that stress is uniform over some spatial extent, slip vectors are oriented in the direction of shear stress on a fault (Wallace 1951; Bott 1959), and that earthquakes occur on pre-existing faults. For details, see reviews by Maury et al. (2013) and Vavryčuk (2014), and references therein. Under these assumptions, the orientation of the principal stress axes (with magnitudes $\sigma_1\sigma_2$, and $\sigma_3$) can be determined, along with the shape ratio $R$ (Gephart and Forsyth 1984) that defines the relative magnitudes of tectonic stress

$$R = \frac{\sigma_1 - \sigma_2}{\sigma_1 - \sigma_3}. \quad (4)$$

In order to apply the assumptions described above, methods for stress inversion from earthquake focal mechanisms typically must distinguish the fault plane from the auxiliary plane. Incorrect fault plane assignment can lead to biased and inaccurate stress inversion results (Michael 1987). For regional tectonic stress inversion presented in this work, we apply the STRESSINVERSE method of Vavryčuk (2014), which solves for fault plane orientations and tectonic stress simultaneously. This method defines the fault plane as the focal mechanism nodal plane that is more unstable within a given stress field orientation (Lund and Slunga 1999), as quantified using the Mohr–Coulomb failure criterion (for critical shear stress $\tau_c$)

$$\tau_c = C + \mu\,(\sigma_n - p)\,. \quad (5)$$

Here, $C$ is fault cohesion, $\mu$ is fault friction, $\sigma_n$ is fault normal stress, and $p$ is pore-fluid pressure. The fault plane is defined as the nodal plane with greater fault failure shear stress (in excess of $\tau_c$) based on the orientation of $\sigma_n$ within a given stress field. Since the technique resolves relative differences between stresses, fault cohesion and pore pressure are not required. Based on laboratory experiments, fault friction $\mu$ typically ranges between 0.6 and 0.8 (Byerlee 1978). Friction can also be considered unknown and solved for as part of this iterative inversion procedure to determine a value that produces the optimal instability for all faults in the focal mechanism dataset. Vavryčuk (2014) demonstrated that the inclusion of this fault-instability criterion yields greater accuracy in the estimated stress shape ratio $R$ compared to previous methods.

The method of Vavryčuk (2014) used in this study initially performs a linear inversion for the stress orientation (Michael 1987) with unknown fault orientation. This is used as an initial estimate to calculate fault instabilities and update the determined fault orientations. These two steps are iterated until convergence. In order to estimate uncertainties in the orientation of the stress field and the shape ratio $R$, the method of Vavryčuk (2014) performs inversions for many realizations of input focal mechanisms with added errors. The uncertainty in the stress parameters are then determined as the maximum differences between the results from the inversion of the original dataset and many realizations of noisy datasets. In their approach, Vavryčuk (2014) assign focal mechanism errors based on a chosen distribution that achieves a desired mean angular deviation for all noisy focal mechanisms in the dataset. This produces errors of arbitrary magnitude and adds errors of the same magnitude for all focal mechanisms in the dataset. In practice, we expect significant differences in the relative errors between different focal mechanism estimates. This can be due to the earthquake magnitude, where larger events generally produce high-SNR waveforms where polarities can be manually assigned more accurately (and at additional, further stations). Site-specific effects may also be important for small events that are only observed on a few stations. Differences in focal mechanism errors can also be attributed to event time, where recent improvements in seismic network coverage lead to improved constraints on earthquake source processes.

In this work, the input focal mechanism data are the set of maximum probability solutions for all probabilistic focal mechanism inversions (as discussed above; Fig. 2). In order to quantify uncertainties in estimated stress parameters, we perform inversions for many realizations of input focal mechanisms, similar to Vavryčuk (2014). However, we employ a data-driven approach to account for focal-mechanism uncertainty. The uncertainty is accounted for by drawing samples from the individual PPDs for each probabilistic focal mechanism inversion. This approach avoids the need to make subjective choices about focal mechanism uncertainties, which are generally difficult to assign a priori. Furthermore, our approach preserves the relative differences in errors between individual focal mechanism estimates. Other methods have been proposed that account for unique focal mechanism errors within stress inversion (e.g., Arnold and Townend 2007; Walsh et al. 2009). However, these approaches rely on assumptions of the underlying distribution of focal mechanism uncertainty. An additional benefit of the approach adopted here is that no such assumption, or error models, are required.

Stress inversion is typically performed for collections of focal mechanisms within some spatial extend where the assumptions discussed above are assumed to be valid. This can involve a series of individual inversions for spatial and (or) temporal clustering of events (e.g., Herrera et al. 2021), or can consist of a single inversion that resolves a model that defines the spatial variability of stress over a region (e.g, Hardebeck

**Fig. 3.** Examples of stress inversion results. (A) Inversion results for spatial window centered at −143° longitude and 60.5° latitude. The histogram shows the distribution of inferred stress shape ratios for 200 bootstrapped inversion results. The lower hemisphere plot shows the orientation of the principal stress axes for the optimal solution (white markers). The red, green, and blue clouds on the lower hemisphere plots represent the distributions of the orientations of $\sigma_1$, $\sigma_2$, and $\sigma_3$, respectively, from 200 bootstrapped inversion results. The opacity of the clouds represent higher probability. (B) Inversion results for spatial window centered at −138° longitude and 61° latitude.

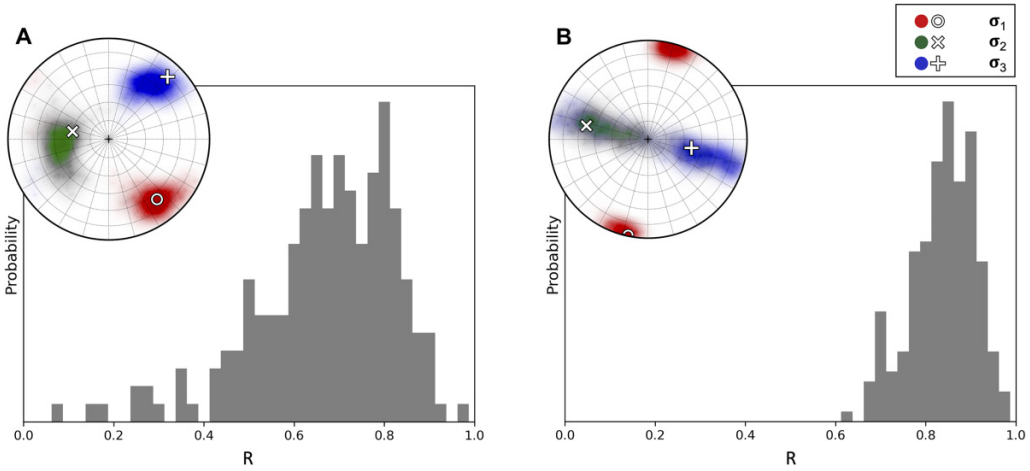


and Michael 2006). However, in the later case, regularization within the inversion procedure precludes propagation of focal mechanism uncertainty into uncertainty of the inferred stress parameters. For simplicity, in this work, we perform stress inversions for overlapping spatial bins (Fig. S10). Bin extents are 2° in longitude, and 1° in latitude. Bin centres are spaced every 1° in longitude, and 0.5° in latitude. However, we only perform stress inversions for bins that contain greater than 15 events. The size and spacing of the bins were chosen as a trade-off between having a sufficient number of input focal mechanisms (for each bin) and the spatial resolution over our study region. Figure 3 shows stress inversion results for two spatial windows centered at the eastern and western edges of our study area, respectively. The lower hemisphere plots illustrate the orientations of the principal stress axes for the optimal solution, as well as the estimated uncertainty determined from 200 bootstrapped inversion results (as detailed above). Similarly, the histograms illustrate the estimated uncertainty in the inferred stress shape ratio $R$ at these two locations in our study region.

## 3. Results and discussion

Using probabilistic earthquake focal mechanisms from this study, in combination with available focal mechanism estimates from the ISC catalog (Lentas et al. 2019), we performed inversions to estimate the orientation of principal stress axes and shape ratios for 31 spatial windows throughout southwestern Yukon and the surrounding region. Figure 4 shows the stress inversion results throughout southwest Yukon. Similar to Fig. 3, the lower hemisphere plots show the orientation of the principal stress axes. The red, green, and blue clouds on the lower hemisphere plots represent the distributions of the orientations of $\sigma_1$, $\sigma_2$, and $\sigma_3$, respectively, from 200 bootstrapped inversion results. To assist in our interpretation, we apply the method of (Lund and Townend 2007) to calculate the orientation of maximum horizontal compressive stress ($\sigma_{\mathrm{Hmax}}$) from our inversion results, which represent partial knowledge of the tectonic stress tensor (Fig. 5A). For each spatial bin, $\sigma_{\mathrm{Hmax}}$ orientations are also computed for 200 bootstrapped inversion results, as a representation of uncertainty. Finally, the inferred stress shape ratios $R$ (a measure of relative stress magnitudes; eq. 1 for each spatial bin are shown in Fig. 5B. Results from previous studies of crustal stress based on earthquake focal mechanisms are also shown (Fig. 5A; Ruppert 2008; Heidbach et al. 2018). Uncertainties in the stress shape ratios, from bootstrapped inversion results, are shown in Fig. S11.

We interpret the stress inversion results for each spatial window as describing the lateral variability of the stress regime. Generally, the stress regime is characterized by the nature of the vertical stress axis, as well as the relative stress magnitudes (quantified by the shape ratio $R$). Specifically, vertical $\sigma_1$, $\sigma_2$, or $\sigma_3$ describe extensional, strike–slip, and compressional regimes, respectively. Throughout the study region, either $\sigma_2$ or $\sigma_3$ is vertical, and $\sigma_1$ is consistently subhorizontal, consistent with an overall transpressive regime. This is expected due to the geometry of the oblique Yakutat convergence at the plate boundary (Fig 1). However, we note significant variations in $\sigma_1$ orientations (Fig. 4). To first order, these orientations are normal to the plate boundary and hence rotate counterclockwise from southeast to northwest in the study region. Inversion results for most spatial windows estimate large shape ratios $R$ (Fig. 5B), suggesting similar magnitudes for $\sigma_2$ and $\sigma_3$ (relative to $\sigma_1$). Furthermore, results for some locations in the region show neither $\sigma_2$ or $\sigma_3$ as vertical. In some cases (e.g., (i) in Fig. 4), uncertainties in $\sigma_2$ and $\sigma_3$ orientations are large. Together, these observations are consistent with an overall transpressive stress regime that exhibits slip partitioning into reverse and thrust

**Fig. 4.** Stress inversions results throughout southwestern Yukon and the surrounding region. The lower hemisphere plots show the orientation of the principal stress axes for each spatial bin. The red, green, and blue clouds on the lower hemisphere plots represent the distributions of the orientations of $\sigma_1$, $\sigma_2$, and $\sigma_3$, respectively, from 200 bootstrapped inversion results. The opacity of the clouds represent higher probability. Examples of large uncertainty in $\sigma_2$ and $\sigma_3$ orientations are illustrated at (i). Examples of vertical $\sigma_3$ and $\sigma_2$ orientations are illustrated at (ii) and (iii), respectively. Faults are labelled as shown in Fig. 1. Figure basemap obtained from ArcGIS mapserver (Esri 2024). Map projection, datum, and coordinates as in Fig. 1.

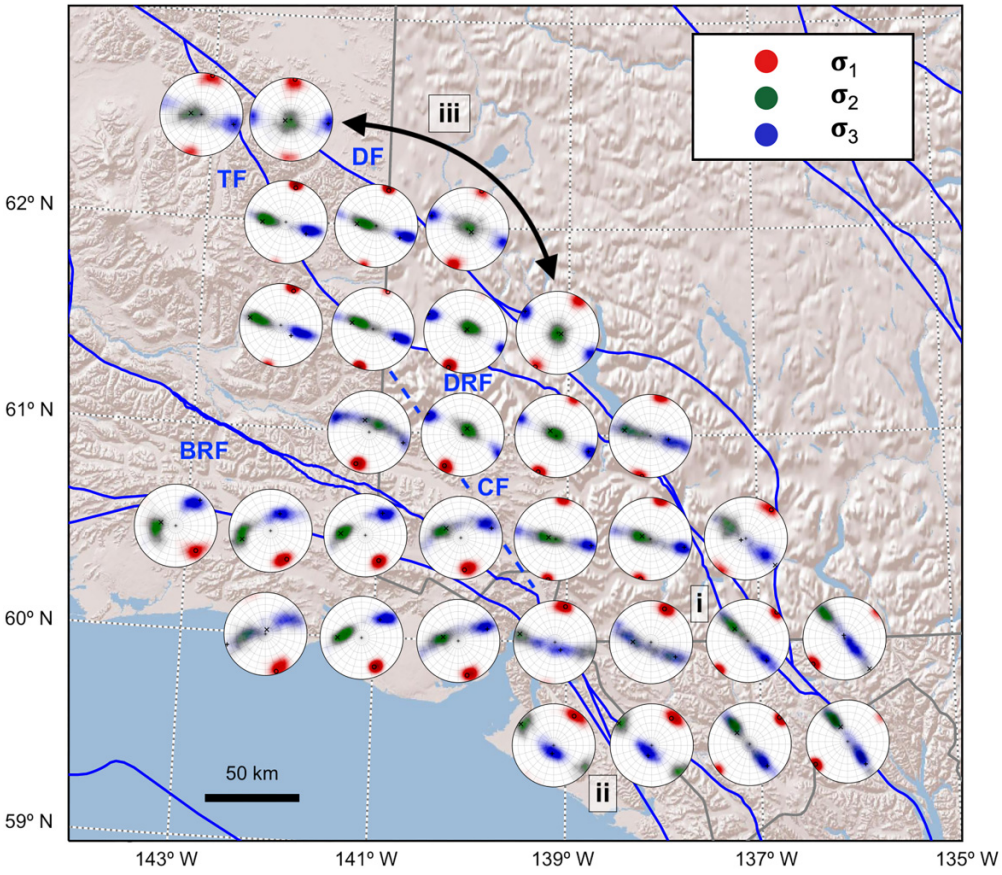


faulting south of the active plate boundary and strike–slip-dominated faulting more inboard, as identified from geological, geomorphological, and seismological observations (e.g., Bemis et al. 2015; Marechal et al. 2018; Biegel et al. 2024).

## 3.1. Spatial variations in crustal stress regime near the Yakutat–North American collision

Overall, our stress inversion results suggest that $\sigma_2$ and $\sigma_3$ are similar in magnitude and form a girdle in the lower hemisphere plots, suggesting overall transpression that allows both reverse and strike–slip motion ((i) in Fig. 4). Local variations within this overall transpressive stress regime are found in the southeastern part of the study region near the Fairweather fault (e.g., region (ii) in Fig. 4). Here, $\sigma_3$ axes are vertical, indicative of a predominantly compressive stress regime. This observation is consistent with the very high rock exhumation rates (>2 km/Myr) indicated by <5 Ma apatite and zircon thermochronology ages (Enkelmann et al. 2015; Falkowski and Enkelmann 2016; Benowitz et al. 2024). The large-magnitude ($M$ > 8) thrust earthquakes with significant surface uplift near Yakutat Bay (Plafker et al. 2008) provide further evidence for high strain-partitioning (Walton et al. 2022). Another variation is observed along the Denali fault in the northern part of the study area with vertical $\sigma_2$ axes and much lower shape ratio estimates ((iii) in Figs. 4 and 5B). These results suggest a predominantly strike–slip stress regime that is consistent with the Holocene strike–slip fault motion suggested by paleoseismology (e.g., Blais-Stevens et al. 2020; Finley et al. 2021) and Quaternary strike–slip rates of 1–2 mm/year (Haeussler et al. 2017; Marechal et al. 2018).

To first order, the trends of $\sigma_1$ and $\sigma_{Hmax}$ are perpendicular to the plate boundary (Fig. 5A). This stress pattern is consistent with the pattern of horizontal crustal motion vectors derived from geodetic data (e.g., Marechal et al. 2015), which radiate normal to the plate boundary at the indenting Yakutat corner. This pattern has been observed at a larger scale across Alaska, and at coarser spatial resolution, from previous studies that predate seismic network improvements (Ruppert 2008; Heidbach et al. 2018). This observation is also apparent further inboard. Specifically, near the Denali fault in the southern part of our study region, $\sigma_{Hmax}$ is oriented perpendicular to the fault ((iv) in Fig. 5A). This suggests unfavourable conditions for strike–slip fault reactiva-

**Fig. 5.** Variations in the orientation of maximum horizontal compressive stress $\sigma_{Hmax}$ (A) and inferred stress shape ratios $R$ (B) throughout southwestern Yukon. Black lines in (A) represent optimal inversion results. Results from 200 bootstrapped inversions are shown in grey. Red lines show the orientations of $\sigma_{Hmax}$ from the World Stress Map Project database (based on formal inversions of focal mechanism clusters; Ruppert 2008; Heidbach et al. 2018). Examples of large estimates of $R$ are illustrated at (iii). Examples of $\sigma_{Hmax}$ orthogonal and oblique to the Denali fault are shown at (iv) and (v), respectively. The abrupt east-to-west transition in $\sigma_{Hmax}$ is shown at (vi). Faults are labelled as shown in Fig. 1. Figure basemap obtained from ArcGIS mapserver (Esri 2024). Map projection, datum, and coordinates as in Fig. 1.

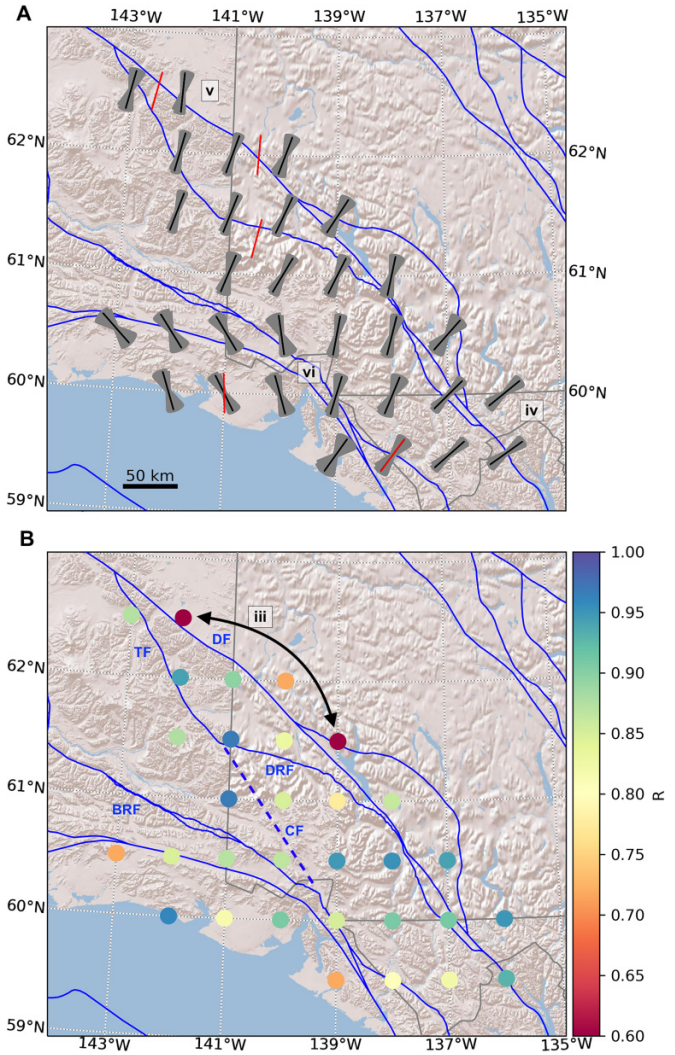


tion, despite the occurrence of large strike–slip earthquakes further outboard along the Fairweather fault (Doser and Lomas 2000). This has been noted by previous studies that examined two recent large-magnitude ($M > 6$) events in this area, which exhibited source properties inconsistent with a strike–slip regime (Choi et al. 2021). Further north along the Denali fault, compressive stress is oriented oblique to the fault, suggesting more favourable conditions for strike–slip motion ((v) in Fig. 5A). This is consistent with estimated reductions in vertical deformation rates, and increases in Denali fault slip rates, from south-to-north within the deformation corridor through southwestern Yukon (Leonard et al. 2007, 2008). These observations are further supported by low-temperature thermochronological studies that indicate high rock exhumation rates (~1 km/Myr) between the Fairweather and Denali faults in the southern part of our study region (approximately between (i) and (ii) in Fig. 4) (e.g., Falkowski and Enkelmann 2016; Enkelmann and Falkowski 2021). These thermochronological studies also suggest that plate motion is accommodated by deformation southwest of the Denali fault (at least in the southern part of our study region) since recent exhumation northeast of the fault is limited. In contrast, the region further north, between the Connector fault and Denali fault, experienced very little rock exhumation (<2–3 km) since Eocene with apatite cooling ages being generally >50 Ma (Enkelmann et al. 2017). Overall, variations in crustal stress based on seismological constraints is in agreement with the concept of strain accumulation near the colliding Yakutat corner, and a pattern radiating from this location (Marechal et al. 2015, 2018).

Our results show an abrupt change in $\sigma_{Hmax}$ orientations from east of the northern end of the Fairweather fault (and the Connector fault) to west of it ((vi) in Fig. 5A). This change in stress orientation coincides with the indenting Yakutat plate corner and the location of the highest peaks and Kluane Ice field (Enkelmann et al. 2015). Though our spatial resolution is reduced due to the windowing approach adopted in this work and low focal mechanism density, we interpret this as the change in stress regime across the Fairweather–Connector–Totschunda fault system. To the east, deformation is characterized by a network of faults within an overall transpressive stress regime (Biegel et al. 2024), with a northeast-trending orientation of compression. To the west, compression is aligned with relative plate motion (northwest), and is attributed to coupling of the overriding plate with the subducting Yakutat slab and an accretionary forearc south the of Border Ranges fault. Figure 1 shows the subsurface extent of the subducting Yakutat slab inferred from seismic imaging (Eberhart-Phillips et al. 2003). More recent studies that merge multiple geophysical datasets, as well as tectonic plate kinematics, estimate the eastern edge of the Yakutat slab to be aligned with the Fairweather–Connector–Totschunda system (Pavlis et al. 2019). The thermal signature of slab-edge magmatism, which contributes to the Wrangell volcanic field (volcanoes in Fig. 1; Trop et al. 2022), may affect or mask the seismic signature of the subducting slab and lead to more complex interpretations of subducting slab geometry. The lack of earthquake focal mechanisms in the immediate vicinity of the southern segment of the Connector fault (Fig. 2) limits our ability to precisely resolve the lateral extent of plate coupling between the Yakutat and North American plates. Furthermore, the southernmost extent of the Connector fault is not well resolved from seismicity (Biegel et al. 2024). Deformation may be more diffuse near the St. Elias syntaxial region (Marechal et al. 2015, 2018) and the various splay faults that stretch parallel to the northern end of the Fairweather fault (e.g., Art Lewis fault and Border Ranges fault; Bruhn

**Fig. 6.** Conceptual model of crustal stress variations near the convergence of the Yakutat microplate with North America. Red arrows illustrate $\sigma_{Hmax}$ orientations. Thick grey lines represent stress regime boundaries. Coloured polygons highlight crustal stress domains. Faults discussed in the text include: Border Ranges fault (BRF), Denali fault (DF), and the Totschunda–Connector–Fairweather fault system (TF-CF-FF). Black arrow shows plate motion vector relative to North America (Kreemer et al. 2014). Blue lines show major faults. Black lines show political boundaries. Inset panels summarize dominant deformation styles within an overall transpressive stress regime, as well as key supporting evidence, including apatite fission track (AFT) thermochronology. References discussed in the text include: (1) Leonard et al. (2007), (2) Marechal et al. (2018), (3) Enkelmann et al. (2017), and (4) Enkelmann and Falkowski (2021). Figure basemap obtained from ArcGIS mapserver (Esri 2024). Map projection, datum, and coordinates as in Fig. 1.

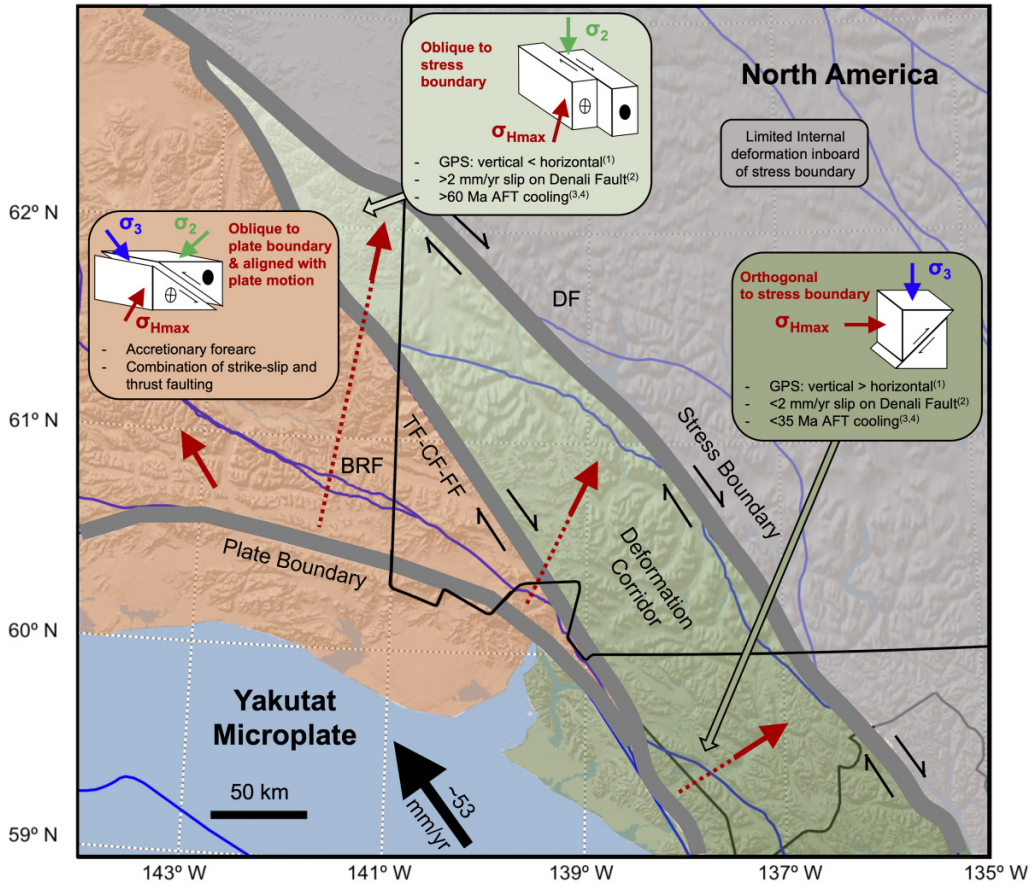


et al. 2012). Three-dimensional numerical modelling of the mechanics of the Yakutat corner convergence suggests localized vertical strain in this orogenic syntaxis, a change from strike–slip to convergence as observed in our work, and the transfer of strain inboard of the plate boundary to connect with the central Denali fault and Alaska Range orogenic system (Koons et al. 2010).

Our main observations and interpretations are summarized by the conceptual model shown in Fig. 6. Specifically, $\sigma_{Hmax}$ orientations are normal to the plate boundary that changes direction at the indenting corner. However, the region north of the plate boundary can be divided into three main domains of stress regimes. These are generally consistent with the main structures in tectonic block models constrained by geodetic data (e.g., Elliott et al. 2010; Elliott and Freymueller 2020). Here, the domains include:

- The western domain (orange in Fig. 6) exhibits coupling of the subducting Yakutat slab with North America that drives crustal stress aligned with relative plate motion and accretion south of the Border Ranges fault. Since plate motion is oblique to the plate boundary, a combination of strike–slip and thrust deformation is observed (with neither vertical $\sigma_2$ or $\sigma_3$). This stress regime continues southward into the Yakutat block itself (Doser et al. 1997).
- The central domain (green in Fig. 6), bounded by the Denali fault to the east and the Totschunda–Connector–Fairweather fault system to the west, represents a deformation corridor that exhibits a spectrum of transpressive stress regime. Variations in crustal stress south-to-north drive progressive variations in horizontal and vertical deformation rates and exhumation. Although the stress regime in this domain is overall transpressive, the southern part exhibits greater reverse deformation (with vertical $\sigma_3$). In contrast, the northern part of this domain exhibits greater strike–slip deformation (with vertical $\sigma_2$). This variation may be due to the location within the domain relative to the orientation of the plate boundary. This may also be

an effect of proximity to the plate boundary. Specifically, there is overall reduced stress transfer driving uplift further inboard from the plate boundary. This spatial variation in stress regime may be further enhanced by deglaciation, which reduces vertical stresses. The Fairweather Range (the southern part of this domain) has been significantly deglaciated, and geodetic data are dominated by the corresponding isostatic adjustment (e.g., Elliott and Freymueller 2020). However, deglaciation is also widespread throughout the region, so this likely does not (entirely) explain our observations.

- Finally, the eastern domain (grey in Fig. 6), further inboard of the Denali fault, shows limited crustal deformation and suggests that the Denali fault acts as a stress boundary. Moderate seismicity and active deformation are observed in the Richardson and Mackenzie Mountains several hundred kilometres further inboard of the plate boundary (outside of our study region). This has led previous studies to suggest that the crust of the North American Cordillera is rigid and transfers strain over these distances via a thermally modulated detachment in the lower crust (e.g., Mazzotti and Hyndman 2002), with implications for regional crustal structure (e.g., Estève et al. 2021; Schutt et al. 2023). The results of this work are constrained by observations of seismicity, which are limited east of the Denali fault (in our study area) and indicate limited (current) internal deformation. Our interpretation is in agreement with the hypothesis of a rigid North American Cordilleran crust. However, our work does not inform on the mechanism of deformation in the Richardson and Mackenzie Mountains. We highlight the alternative hypothesis that the Northern Cordillera is a rigid lithospheric block, and that convergence at its eastern boundary (where it collides with the North American craton) involves slip on lithospheric faults. Furthermore, stress may be transferred by the craton via the opening of the North Atlantic (Enkelmann et al. 2019; McKay et al. 2021). This remains an unresolved tectonic question.

## 4. Conclusions

This study presents estimates of the orientation and shape ratio of stress in the North American crust throughout southwestern Yukon and the surrounding region. Stress parameters are inferred via inversion of earthquake focal mechanisms located within spatial windows throughout the study area. The earthquake focal mechanisms were inferred from P-wave polarity measurements that leverage improvements in regional seismic station networks in the area over the last decades. In general, seismicity throughout the region is dominated by reverse and dextral strike–slip faulting. Many earthquake focal mechanisms considered in this study are small-magnitude, poorly constrained events. However, solutions are inferred within a probabilistic framework that rigorously quantifies focal mechanism uncertainties. As a result, these focal mechanisms are able to provide valuable information for constraining tectonic stresses. We implement a novel, data-driven approach to propagate focal mechanism uncertainty in stress inversion. The earthquake focal mechanisms and stress inversion results significantly improve upon existing sparse information in this region.

Overall, southeastern Alaska and southwestern Yukon are characterized by a transpressive stress regime. Yet, orientations of compressive stress are approximately normal to the margin and rotate counterclockwise from south to north following the indenting Yakutat plate corner. Stress inversion results reveal an abrupt change in orientation, which we interpret as a change in stress regime across the Fairweather–Connector–Totschunda fault system that is likely related to coupling between the subducting Yakutat slab and North America. Overall, the stress pattern is consistent with geodetically derived vectors of crustal deformation. Our interpretation is consistent with geological, geomorphological, and seismological constraints on deformation and fault slip throughout the region. The spatial pattern of Cenozoic rock exhumation, which results from uplift and erosion over millions of years, is also in agreement with the observed change of reverse to strike–slip-dominated deformation within the central domain of the study region (Fig. 6).

This work is part of a larger, multiyear study of natural hazards and geothermal resource potential in Yukon. The estimation of stress orientations and relative magnitudes has implications for potential fault instability, as well as fault permeability. Results from this study enable more detailed examination of kinematics of the Denali fault and surrounding fault systems throughout southwestern Yukon. Our results represent an estimate of the current state of crustal stress based on more than a decade of available seismic data. The role of stress evolution, including within multicentury cycles of great earthquakes, is beyond the scope of our analysis. Southwestern Yukon and surrounding regions exhibit complex tectonic deformation that likely continues to evolve in the present day.

## Acknowledgements

We thank Kluane First Nation for their support of this research. We also thank Carlos Herrera and Mahdi Hamidbeygi for useful discussions on focal mechanism and stress inversions. We thank two anonymous reviewers for their valuable feedback of the initial manuscript. This is Yukon Geological Survey contribution #069.

## Article information

### History dates

Received: 24 June 2024
Accepted: 24 September 2024
Accepted manuscript online: 15 October 2024
Version of record online: 6 December 2024

### Notes

This paper is part of a Special Issue entitled Geophysical studies of the lithosphere and plate boundaries in honour of Roy D. Hyndman.

## Data availability
All seismic data used in this work are freely available for download through the international Federation of Digital Seismograph Networks (FDSN) Web Services of the facilities of the Incorporated Research Institutions for Seismology (IRIS; https://service.iris.edu/). Data were downloaded and processed using ObsPy (Beyreuther et al. 2010), and polarities were manually assigned using Pyrocko/Snuffler (Heimann et al. 2017). Stress inversions were performed using STRESSINVERSE software (Vavryčuk 2014). Maps throughout this work use mapserver basemaps available through ArcGIS software by Esri. ArcGIS is the intellectual property of Esri and is used herein under license. Copyright Esri. All rights reserved. For more information about Esri software, please visit www.esri.com.

# Author information

## Author ORCIDs
Jeremy M. Gosselin https://orcid.org/0000-0002-0375-4102
Katherine M. Biegel https://orcid.org/0000-0001-8682-6169
Jan Dettmer https://orcid.org/0000-0001-8906-8156
Hersh Gilbert https://orcid.org/0000-0002-7446-3898
Maurice Colpron https://orcid.org/0000-0002-4207-8215
Eva Enkelmann https://orcid.org/0000-0002-1988-0760

## Author contributions
Conceptualization: JMG, KMB, JD
Data curation: JMG
Formal analysis: JMG
Funding acquisition: JMG
Investigation: JMG, KMB, JD, GH, MC, EE
Methodology: JMG, JD
Project administration: JMG, JD, GH, MC
Resources: JMG
Software: JMG
Validation: JMG, KMB, JD, MC, EE
Visualization: JMG
Writing – original draft: JMG
Writing – review & editing: JMG, KMB, JD, GH, MC, EE

## Competing interests
The authors declare there are no competing interests.

## Funding information
This work was supported by the Natural Science and Engineering Research Council (Canada) through a Postdoctoral Fellowship to JMG and a Discovery Grant to JD, and Alliance Grant ALLRP-80887-22. This work is also supported by the Yukon Geological Survey through funding from Natural Resources Canada's Emerging Renewal Power Program and the Yukon government's Our Clean Future initiative.

# Supplementary material

Supplementary data are available with the article at https://doi.org/10.1139/cjes-2024-0095.

# References

Alaska Earthquake Center 1987. University of Alaska Fairbanks, Alaska Geophysical Network. Available from https://www.fdsn.org/networks/detail/AK/ [accessed 1 October 2022].

Álvarez-Gómez, J.A. 2019. FMC'Earthquake focal mechanisms data management, cluster and classification. SoftwareX, **9**: 299–307. doi:10.1016/j.softx.2019.03.008.

Arnold, R., and Townend, J. 2007. A Bayesian approach to estimating tectonic stress from seismological data. Geophysical Journal International, **170**(3): 1336–1356. doi:10.1111/j.1365-246X.2007.03485.x.

Baker, M.G., Heath, D.C., Schutt, D.L., Aster, R.C., Cubley, J.F., and Freymueller, J.T. 2020. The Mackenzie Mountains EarthScope Project: studying active deformation in the northern North American Cordillera from margin to craton. Seismological Research Letters, **91**(1): 521–532. doi:10.1785/0220190139.

Bemis, S.P., Weldon, R.J., and Carver, G.A. 2015. Slip partitioning along a continuously curved fault: Quaternary geologic controls on Denali fault system slip partitioning, growth of the Alaska Range, and the tectonics of south-central Alaska. Lithosphere, **7**(3): 235–246. doi:10.1130/L352.1.

Benowitz, J.A., Lease, R., Haeussler, P.J., Pavlis, T., and Mann, M.E. 2024. Fairweather transform boundary Oligocene to present orogenesis: Fairweather Range vertical extrusion and rotation of the Yakutat microplate at ca. 3 Ma. Tectonophysics, **880**: 230337.

Beyreuther, M., Barsch, R., Krischer, L., Megies, T., Behr, Y., and Wassermann, J. 2010. ObsPy: a Python toolbox for seismology. Seismological Research Letters, **81**(3): 530–533. doi:10.1785/gssrl.81.3.530.

Biegel, K.M., Gosselin, J.M., Dettmer, J., Colpron, M., Enkelmann, E., and Caine, J.S. 2024. Earthquake relocations delineate a discrete fault network and deformation corridor throughout southeast Alaska and southwest Yukon. Tectonics, **43**(5): e2023TC008140. doi:10.1029/2023TC008140.

Blais-Stevens, A., Clague, J.J., Brahney, J., Lipovsky, P., Haeussler, P.J., and Menounos, B. 2020. Evidence for large Holocene earthquakes along the Denali fault in southwest Yukon, Canada. Environmental & Engineering Geoscience, **26**(2): 149–166. doi:10.2113/EEG-2263.

Bott, M.H.P. 1959. The mechanics of oblique slip faulting. Geological Magazine, **96**(2): 109–117. doi:10.1017/S0016756800059987.

Brillinger, D., Udias, A., and Bolt, B. 1980. A probability model for regional focal mechanism solutions. Bulletin of the Seismological Society of America, **70**(1): 149–170. doi:10.1785/BSSA0700010149.

Bruhn, R.L., Sauber, J., Cotton, M.M., Pavlis, T.L., Burgess, E., Ruppert, N., and Forster, R.R. 2012. Plate margin deformation and active tectonics along the northern edge of the Yakutat Terrane in the Saint Elias Orogen, Alaska, and Yukon, Canada. Geosphere, **8**(6): 1384–1407. doi:10.1130/GES00807.1.

Busby, R.W., and Aderhold, K. 2020. The Alaska transportable array: as built. Seismological Research Letters, **91**(6): 3017–3027. doi:10.1785/0220200154.

Byerlee, J. 1978. Friction of rocks. *In* Rock friction and earthquake prediction, Birkhäuser Basel, Basel. pp. 615–626. doi:10.1007/978-3-0348-7182-2_4.

Choi, M., Eaton, D.W., and Enkelmann, E. 2021. Is the Eastern Denali fault still active? Geology, **49**(6): 662–666. doi:10.1130/G48461.1.

Christeson, G.L., Gulick, S.P., van Avendonk, H.J., Worthington, L.L., Reece, R.S., and Pavlis, T.L. 2010. The Yakutat terrane: dramatic change in crustal thickness across the Transition fault, Alaska. Geology, **38**(10): 895–898. doi:10.1130/G31170.1.

Del Moral, P., Doucet, A., and Jasra, A. 2006. Sequential Monte Carlo samplers. Journal of the Royal Statistical Society Series B: Statistical Methodology, **68**(3): 411–436. doi:10.1111/j.1467-9868.2006.00553.x.

Doser, D.I. 2014. Seismicity of southwestern Yukon, Canada, and its relation to slip transfer between the Fairweather and Denali fault systems. Tectonophysics, **611**: 121–129. doi:10.1016/j.tecto.2013.11.018.

Doser, D.I., and Lomas, R. 2000. The transition from strike–slip to oblique subduction in southeastern Alaska from seismological studies. Tectonophysics, **316**(1–2): 45–65. doi:10.1016/S0040-1951(99)00254-1.

Doser, D.I., Pelton, J.R., and Veilleux, A.M. 1997. Earthquakes in the Pamplona zone, Yakutat block, south central Alaska. Journal of Geophysical Research: Solid Earth, **102**(B11): 24499–24511. doi:10.1029/97JB01729.

Eberhart-Phillips, D., Haeussler, P.J., Freymueller, J.T., Frankel, A.D., Rubin, C.M., Craw, P., Ratchkovski, N.A., Anderson, G., et al. 2003. The 2002 Denali fault earthquake, Alaska: a large magnitude, slip-partitioned event. Science, **300**(5622): 1113–1118. doi:10.1126/science.1082703.

Eberhart-Phillips, D., Christensen, D.H., Brocher, T.M., Hansen, R., Ruppert, N.A., Haeussler, P.J., and Abers, G.A. 2006. Imaging the transition from Aleutian subduction to Yakutat collision in central Alaska, with local earthquakes and active source data. Journal of Geophysical Research: Solid Earth, **111**(B11). doi:10.1029/2005JB004240.

Eisbacher, G. 1976. Sedimentology of the Dezadeash flysch and its implications for strike–slip faulting along the Denali fault, Yukon Territory and Alaska. Canadian Journal of Earth Sciences, **13**(11): 1495–1513. doi:10.1139/e76-157.

Ekström, G., Nettles, M., and Dziewoński, A. 2012. The global CMT project 2004–2010: centroid-moment tensors for 13,017 earthquakes. Physics of the Earth and Planetary Interiors, **200**: 1–9. doi:10.1016/j.pepi.2012.04.002.

Elliott, J., and Freymueller, J.T. 2020. A block model of present-day kinematics of Alaska and western Canada. Journal of Geophysical Research: Solid Earth, **125**(7): e2019JB018378. doi:10.1029/2019JB018378.

Elliott, J.L., Larsen, C.F., Freymueller, J.T., and Motyka, R.J. 2010. Tectonic block motion and glacial isostatic adjustment in southeast Alaska and adjacent Canada constrained by GPS measurements. Journal of Geophysical Research: Solid Earth, **115**(B9). doi:10.1029/2009JB007139.

Enkelmann, E., and Falkowski, S. 2021. Deformation between the highly oblique Yakutat–North American plate boundary and the Eastern Denali fault. Geosphere, **17**(6): 2123–2143. doi:10.1130/GES02410.1.

Enkelmann, E., Garver, J.I., and Pavlis, T.L. 2008. Rapid exhumation of ice-covered rocks of the Chugach–St. Elias orogen, Southeast Alaska. Geology, **36**(12): 915–918. doi:10.1130/G2252A.1.

Enkelmann, E., Zeitler, P., Pavlis, T., Garver, J., and Ridgway, K. 2009. Intense localized rock uplift and erosion in the St Elias orogen of Alaska. Nature Geoscience, **2**(5): 360–363. doi:10.1038/ngeo502.

Enkelmann, E., Koons, P.O., Pavlis, T.L., Hallet, B., Barker, A., Elliott, J., et al. 2015. Cooperation among tectonic and surface processes in the St. Elias Range, Earth's highest coastal mountains. Geophysical Research Letters, **42**(14): 5838–5846. doi:10.1002/2015GL064727.

Enkelmann, E., Piestrzeniewicz, A., Falkowski, S., Stübner, K., and Ehlers, T.A. 2017. Thermochronology in southeast Alaska and southwest Yukon: implications for North American Plate response to terrane accretion. Earth and Planetary Science Letters, **457**: 348–358. doi:10.1016/j.epsl.2016.10.032.

Enkelmann, E., Finzel, E., and Arkle, J. 2019. Deformation at the eastern margin of the Northern Canadian Cordillera: potentially related to opening of the North Atlantic. Terra Nova, **31**(3): 151–158. doi:10.1111/ter.12374.

Esri. 2024. World Mapserver compiled by Esri, Garmin, GEBCO, NOAA NGDC, and other contributors, scale not given. Available from https://server.arcgisonline.com/arcgis/rest/services/ [accessed March 2024].

Estève, C., Gosselin, J., Audet, P., Schaeffer, A., Schutt, D., and Aster, R. 2021. Surface-wave tomography of the northern Canadian Cordillera using earthquake Rayleigh wave group velocities. Journal of Geophysical Research: Solid Earth, **126**(8): e2021JB021960. doi:10.1029/2021JB021960.

Falkowski, S., and Enkelmann, E. 2016. Upper-crustal cooling of the wrangellia composite terrane in the northern St. Elias mountains, western canada. Lithosphere, **8**(4): 359–378. doi:10.1130/L508.1.

Finley, T., Salomon, G., Nissen, E., Stephen, R., Cassidy, J., and Menounos, B. 2021. Preliminary results and structural interpretations from drone lidar surveys over the Eastern Denali fault, Yukon. *In* Yukon Exploration and Geology. *Edited by* K.E. MacFarlane. Yukon Geological Survey. pp. 83–105.

Finzel, E.S., Trop, J.M., Ridgway, K.D., and Enkelmann, E. 2011. Upper plate proxies for flat-slab subduction processes in southern Alaska. Earth and Planetary Science Letters, **303**(3–4): 348–360. doi:10.1016/j.epsl.2011.01.014.

Fogleman, K.A., Lahr, J.C., Stephens, C.D., and Page, R.A. 1993. Earthquake locations determined by the southern Alaska seismograph network for October 1971 through May 1989. US Geological Survey Open-File Report 93-309. 54p. doi:10.3133/ofr93309.

Gephart, J.W., and Forsyth, D.W. 1984. An improved method for determining the regional stress tensor using earthquake focal mechanism data: application to the San Fernando earthquake sequence. Journal of Geophysical Research: Solid Earth, **89**(B11): 9305–9320. doi:10.1029/JB089iB11p09305.

Global Volcanism Program. 2024. Volcanoes of the World (v. 5.1.7; 26 April 2024). Distributed by Smithsonian Institution, compiled by Venzke, E. doi:10.5479/si.GVP.VOTW5-2023.5.1.

Gosselin, J.M., Biegel, K., Hamidbeygi, M., and Dettmer, J. 2022. Improvements in the regional earthquake focal mechanism catalogue for southwestern Yukon. *In* Yukon exploration and geology. *Edited by* K.E. MacFarlane. Yukon Geological Survey. pp. 63–76.

Haeussler, P.J., Matmon, A., Schwartz, D.P., and Seitz, G.G. 2017. Neotectonics of interior Alaska and the late Quaternary slip rate along the Denali fault system. Geosphere, **13**(5): 1445–1463. doi:10.1130/GES01447.1.

Hamidbeygi, M. 2022. Nonlinear Bayesian estimation of centroid moment tensors using multiple seismic data sets in the Kiskatinaw seismic monitoring and mitigation area.

Han, J., Dettmer, J., Gosselin, J.M., Gilbert, H., Biegel, K., and Kim, S. 2024. Seismicity near the eastern Denali fault from temporary and long-term seismic recordings. *In* Yukon Exploration and Geology Technical Papers 2023. *Edited by* L.H. Weston. Yukon Geological Survey. pp. 37–50.

Hardebeck, J.L., and Michael, A.J. 2006. Damped regional-scale stress inversions: methodology and examples for southern California and the Coalinga aftershock sequence. Journal of Geophysical Research: Solid Earth, **111**(B11). doi:10.1029/2005JB004144.

Hayes, G.P., Moore, G.L., Portner, D.E., Hearne, M., Flamme, H., Furtney, M., and Smoczyk, G.M. 2018. Slab2, a comprehensive subduction zone geometry model. Science, **362**(6410): 58–61. doi:10.1126/science.aat4723.

Heidbach, O., Rajabi, M., Cui, X., Fuchs, K., Müller, B., Reinecker, J., et al. 2018. The World Stress Map database release 2016: crustal stress pattern across scales. Tectonophysics, **744**: 484–498. doi:10.1016/j.tecto.2018.07.007.

Heimann, S., Kriegerowski, M., Isken, M., Cesca, S., Daout, S., Grigoli, F., et al. 2017. Pyrocko: a versatile seismology toolkit for Python. Available from http://pyrocko.org [accessed 1 March 2022].

Herrera, C., Cassidy, J.F., Dosso, S.E., Dettmer, J., Bloch, W., Sippl, C., and Salazar, P. 2021. The crustal stress field inferred from focal mechanisms in northern Chile. Geophysical Research Letters, **48**(8): e2021GL092889. doi:10.1029/2021GL092889.

Jaynes, E.T. 2003. Probability theory: the logic of science. Cambridge university press.

Kagan, Y. 1991. 3-D rotation of double-couple earthquake sources. Geophysical Journal International, **106**(3): 709–716. doi:10.1111/j.1365-246X.1991.tb06343.x.

Kao, H., Shan, S.J., Bent, A., Woodgold, C., Rogers, G., Cassidy, J.F., and Ristau, J. 2012. Regional centroid–moment–tensor analysis for earthquakes in Canada and adjacent regions: an update. Seismological Research Letters, **83**(3): 505. doi:10.1785/gssrl.83.3.505.

Kaverina, A., Lander, A., and Prozorov, A. 1996. Global creepex distribution and its relation to earthquake-source geometry and tectonic origin. Geophysical Journal International, **125**(1): 249–265. doi:10.1111/j.1365-246X.1996.tb06549.x.

Koons, P.O., Hooks, B., Pavlis, T., Upton, P., and Barker, A. 2010. Three-dimensional mechanics of Yakutat convergence in the southern Alaskan plate corner. Tectonics, **29**(4). doi:10.1029/2009TC002463.

Koons, P.O., Hallet, B., Zeitler, P.K., and Meltzer, A.S. 2022. Tectonic Aneurysm: a culmination of tectonic and geomorphic cooperation in mountain building. *In* Treatise on geomorphology. 2nd ed. *Edited by* J.J.F. Shroder. Academic Press, Oxford. pp. 695–

728. Available from https://www.sciencedirect.com/science/article/pii/B9780128182345001796 [accessed 1 November 2022]. doi:10.1016/B978-0-12-818234-5.00179-6.

Kreemer, C., Blewitt, G., and Klein, E.C. 2014. A geodetic plate motion and Global Strain Rate Model. Geochemistry, Geophysics, Geosystems, **15**(10): 3849–3889. doi:10.1002/2014GC005407.

Lahr, J.C., and Plafker, G. 1980. Holocene Pacific–North American plate interaction in southern Alaska: implications for the Yakataga seismic gap. Geology, **8**(10): 483–486. doi:10.1130/0091-7613(1980)8⟨483:HPAPII⟩2.0.CO;2.

Lentas, K., Di Giacomo, D., Harris, J., and Storchak, D.A. 2019. The ISC Bulletin as a comprehensive source of earthquake source mechanisms. Earth System Science Data, **11**(2): 565–578. doi:10.5194/essd-11-565-2019.

Leonard, L.J., Hyndman, R.D., Mazzotti, S., Nykolaishen, L., Schmidt, M., and Hippchen, S. 2007. Current deformation in the northern Canadian Cordillera inferred from GPS measurements. Journal of Geophysical Research: Solid Earth, **112**(B11). doi:10.1029/2007JB005061.

Leonard, L.J., Mazzotti, S., and Hyndman, R.D. 2008. Deformation rates estimated from earthquakes in the northern Cordillera of Canada and eastern Alaska. Journal of Geophysical Research: Solid Earth, **113**(B8). doi:10.1029/2007JB005456.

Lowey, G.W. 1998. A new estimate of the amount of displacement on the Denali fault system based on the occurrence of carbonate megaboulders in the Dezadeash Formation (Jura–Cretaceous), Yukon, and the Nutzotin Mountains sequence (Jura–Cretaceous), Alaska. Bulletin of Canadian Petroleum Geology, **46**(3): 379–386.

Lund, B., and Slunga, R. 1999. Stress tensor inversion using detailed microearthquake information and stability constraints: application to Ölfus in southwest Iceland. Journal of Geophysical Research: Solid Earth, **104**(B7): 14947–14964. doi:10.1029/1999JB900111.

Lund, B., and Townend, J. 2007. Calculating horizontal stress orientations with full or partial knowledge of the tectonic stress tensor. Geophysical Journal International, **170**(3): 1328–1335. doi:10.1111/j.1365-246X.2007.03468.x.

MacKay, D.J. 2003. Information theory, inference and learning algorithms. Cambridge University Press.

Marechal, A., Mazzotti, S., Elliott, J.L., Freymueller, J.T., and Schmidt, M. 2015. Indentor-corner tectonics in the Yakutat–St. Elias collision constrained by GPS. Journal of Geophysical Research: Solid Earth, **120**(5): 3897–3908. doi:10.1002/2014JB011842.

Marechal, A., Ritz, J.F., Ferry, M., Mazzotti, S., Blard, P.H., Braucher, R., and Saint-Carlier, D. 2018. Active tectonics around the Yakutat indentor: new geomorphological constraints on the eastern Denali, Totschunda and Duke River Faults. Earth and Planetary Science Letters, **482**: 71–80. doi:10.1016/j.epsl.2017.10.051.

Maury, J., Cornet, F.H., and Dorbath, L. 2013. A review of methods for determining stress fields from earthquakes focal mechanisms; application to the Sierentz 1980 seismic crisis (Upper Rhine graben). Bulletin de la Societe Geologique de France, **184**(4–5): 319–334. doi:10.2113/gssgfbull.184.4-5.319.

Mazzotti, S., and Hyndman, R.D. 2002. Yakutat collision and strain transfer across the northern Canadian Cordillera. Geology, **30**(6): 495–498. doi:10.1130/0091-7613(2002)030⟨0495:YCASTA⟩2.0.CO;2.

McDermott, R.G., Ault, A.K., Caine, J.S., and Thomson, S.N. 2019. Thermotectonic history of the Kluane Ranges and evolution of the eastern Denali fault zone in southwestern Yukon, Canada. Tectonics, **38**(8): 2983–3010. doi:10.1029/2019TC005545.

McKay, R., Enkelmann, E., Hadlari, T., Matthews, W., and Mouthereau, F. 2021. Cenozoic exhumation history of the eastern margin of the Northern Canadian Cordillera. Tectonics, **40**(4): e2020TC006582. doi:10.1029/2020TC006582.

McKenzie, D.P. 1969. The relation between fault plane solutions for earthquakes and the directions of the principal stresses. Bulletin of the Seismological Society of America, **59**(2): 591–601. doi:10.1785/BSSA0590020591.

Meighan, L.N., Cassidy, J.F., Mazzotti, S., and Pavlis, G.L. 2013. Microseismicity and tectonics of southwest Yukon Territory, Canada, using a local dense seismic array. Bulletin of the Seismological Society of America, **103**(6): 3341–3346. doi:10.1785/0120130068.

Michael, A.J. 1987. Use of focal mechanisms to determine stress: a control study. Journal of Geophysical Research: Solid Earth, **92**(B1): 357–368. doi:10.1029/JB092iB01p00357.

Nelson, J.L., Colpron, M., and Israel, S. 2013. The cordillera of British Columbia, Yukon, and Alaska: tectonics and metallogeny. *In* Tectonics, metallogeny and discovery: the North American Cordillera and similar accretionary settings 17. *Edited by* M. Colpron, T. Bissig, B.G. Rusk and J.F.H. Thompson. Society of Economic Geologists, Inc., Special Publicatio. pp. 53–103.

Pavlis, G.L., Bauer, M.A., Elliott, J.L., Koons, P., Pavlis, T.L., Ruppert, N., Ward, K.M., and Worthington, L.L. 2019. A unified three-dimensional model of the lithospheric structure at the subduction corner in southeast Alaska: summary results from STEEP. Geosphere, **15**(2): 382–406. doi:10.1130/GES01488.1.

Plafker, G. 1987. Regional geology and petroleum potential of the northern Gulf of Alaska continental margin. *In* Geology and resource potential of the continental margin of western north America and adjacent ocean basins—Beaufort sea to Baja California, 6. pp. 229–268.

Plafker, G., Thatcher, W., Freymueller, J., Haeussler, P., Wesson, R., and Ekström, G. 2008. Geological and geophysical evaluation of the mechanisms of the great 1899 Yakutat Bay earthquakes. *In* Active tectonics and seismic potential of Alaska 179. pp. 215–236. doi:10.1029/179GM12.

Richter, D., and Matson, N., Jr., 1971. Quaternary faulting in the eastern Alaska Range. Geological Society of America Bulletin, **82**(6): 1529–1540. doi:10.1130/0016-7606(1971)82[1529:QFITEA]2.0.CO;2.

Ristau, J., Rogers, G.C., and Cassidy, J.F. 2007. Stress in western Canada from regional moment tensor analysis. Canadian Journal of Earth Sciences, **44**(2): 127–148. doi:10.1139/e06-057.

Ruppert, N.A. 2008. Stress map for Alaska from earthquake focal mechanisms. *In* Active tectonics and seismic potential in Alaska, Geophysical Monograph Series, 179. *Edited by* J.T. Freymueller, P.J. Haeussler, R.L. Wesson and G. Ekström. pp. 351–367. doi:10.1029/179GM20.

Ruppert, N.A., and West, M.E. 2020. The impact of USArray on earthquake monitoring in Alaska. Seismological Research Letters, **91**(2A): 601–610. doi:10.1785/0220190227.

Schutt, D.L., Porritt, R.W., Estève, C., Audet, P., Gosselin, J.M., Schaeffer, A.J., et al. 2023. Lithospheric S wave velocity variations beneath the Mackenzie Mountains and Northern Canadian Cordillera. Journal of Geophysical Research: Solid Earth, **128**(1): e2022JB025517. doi:10.1029/2022JB025517.

Trop, J.M., Benowitz, J.A., Kirby, C.S., and Brueseke, M.E. 2022. Geochronology of the Wrangell Arc: spatial–temporal evolution of slab-edge magmatism along a flat-slab, subduction–transform transition, Alaska–Yukon. Geosphere, **18**(1): 19–48. doi:10.1130/GES02417.1.

Vasyura-Bathke, H., Dettmer, J., Steinberg, A., Heimann, S., Isken, M.P., Zielke, O., et al. 2020. The Bayesian earthquake analysis tool. Seismological Research Letters, **91**(2A): 1003–1018. doi:10.1785/0220190075.

Vavryčuk, V. 2014. Iterative joint inversion for stress and fault orientations from focal mechanisms. Geophysical Journal International, **199**(1): 69–77. doi:10.1093/gji/ggu224.

Wallace, R.E. 1951. Geometry of shearing stress and relation to faulting. The Journal of geology, **59**(2): 118–130. doi:10.1086/625831.

Walsh, D., Arnold, R., and Townend, J. 2009. A Bayesian approach to determining and parametrizing earthquake focal mechanisms. Geophysical Journal International, **176**(1): 235–255. doi:10.1111/j.1365-246X.2008.03979.x.

Walton, M.A., Gulick, S.P., and Haeussler, P.J. 2022. Revisiting the 1899 earthquake series using integrative geophysical analysis in Yakutat Bay, Alaska, USA. Geosphere, **18**(5): 1453–1473. doi:10.1130/GES02423.1.

Worthington, L.L., Daigle, H., Clary, W.A., Gulick, S.P., and Montelli, A. 2018. High sedimentation rates and thrust fault modulation: insights from ocean drilling offshore the St. Elias Mountains, southern Alaska. Earth and Planetary Science Letters, **483**: 1–12. doi:10.1016/j.epsl.2017.11.041.